Research Article | Vol. 32, No. 7 / 25 Mar 2024 / Optics Express 12127
Optics EXPRESS

Quadrupole excitation of atoms with tightly focused Laguerre-Gaussian beams

LEILA MASHHADI[1,3] AND GHOLAMREZA SHAYEGANRAD[2,4]

[1]Independent Researcher, 206 Millbrook Road East, Southampton, SO151JS, UK
[2]Optoelectronics Research Centre, University of Southampton, Southampton, SO17 1BJ, UK
[3]leila.mashhadi@yahoo.com
[4]g.shayeganrad@soton.ac.uk

Abstract: This article investigates the quadrupole excitation of a trapped atom exposed to the tightly focused Laguerre-Gaussian (LG) beams with parallel and antiparallel spin angular momentum (SAM) and orbital angular momentum (OAM) under nonparaxial conditions. The Rabi frequency profile of allowed quadrupole transition channels, modified by SAM and OAM interaction, in the focal plane is provided. In the case of antiparallel SAM and OAM, the excitation probability undergoes substantial modification due to the considerable contribution of longitudinal intensity variations in tightly focused condition. The findings offer insights into controlling localized atom transition, including OAM transfer, with potential applications in qudit-based technologies.

1. Introduction

The precise focusing of laser beams using high numerical aperture lenses has found extensive applications in the optical manipulation and control of micro- and nano-particles [1]. This technique has been particularly valuable in addressing and individually manipulating the positions and quantum states of localized atoms within diverse atom-light interaction processes [2–5]. In the pursuit of expanding the practical application of localized atoms into large-scale quantum nodes, researchers have delved into a variety of techniques, including the utilization of tightly focused structured beams [6,7], enabling precise control and manipulation of quantum states within assemblies of atoms. This novel approach substantially impacts the advancement of quantum computing, quantum communication, and quantum simulation [8–10].

Among the structured beams, dark-centered Laguerre-Gaussian (LG) beams have emerged as crucial tools in atom-light interactions [11–14]. They have frequently been employed in innovative theoretical and experimental approaches, especially in the field of neutral atom-based quantum information, where the aim is to enhance transmission capacity while maintaining high operational fidelity [15]. The LG beams, blue detuned from the atomic resonance, in particular, are capable of confining atomic qudits within the dark central region of the beam [16,17]. This effectively shields the atoms from laser-induced noises, to preserve coherence in trapped atoms allowing them to compete favorably with superconducting circuits [18] and trapped ions [19]. When these beams are tightly focused, they exhibit wavelength-scale intensity variations in the focal plane, which can be utilized for spatially controlling of the quadrupole excitation of trapped atoms. This intriguing feature holds promise for applications in high-dimensional quantum information protocols [12]. However, the nonparaxial characteristics of tightly focused LG beams can influence the interaction with trapped atoms in the focal region, extending beyond the conventional paraxial approximation. In this regard, the quadrupole excitation of ions using polarized LG beams through the analytic solution in the Lorentz gauge previously investigated [20]. Nonetheless, a modified theoretical framework that offers a complete overview

#500848 https://doi.org/10.1364/OE.500848
Journal © 2024 Received 14 Sep 2023; revised 21 Dec 2023; accepted 18 Jan 2024; published 19 Mar 2024

Optics EXPRESS

of quadrupole excitation in tightly focused LG beams, considering orbital angular momentum (OAM) and spin angular momentum (SAM) interaction in the focal region, and detailing the impact of focusing parameters on quadrupole interaction, could prove advantages for practical applications.

Polarized LG modes represent eigenfunctions of both OAM operator, characterized by quantum numbers $l = 0, \pm 1, \pm 2 \ldots$, defining the spatial inhomogeneity of the beam, and SAM operator, with spin quantum numbers $\sigma = \pm 1$, contributing to the total angular momentum, $l + \sigma$ [21,22]. Under the paraxial approximation, SAM and OAM are considered relatively independent degrees of freedom and manipulated separately. SAM is associated with the electronic state transitions of atoms through dipole interactions, while OAM influences the center-of-mass motion of atoms and can alter standard selection rules in higher-order quadrupole transitions [23]. This capability extends traditional qubit protocols to high-dimensional quantum information, known as qudits [24–26]. In contrast, under nonparaxial conditions of tightly focused LG beams, SAM and OAM are coupled, as evidenced by the spin-dependent intensity distributions of the focused LG beams [27,28]. This induces SAM-to-OAM conversion, significantly impacting selection rules and transition strengths in the interaction of such beams with atoms, and enabling a range of functionalities in various applications, particularly within neutral atom-based quantum information processing. Furthermore, the generation, manipulation, and detection of combined SAM and OAM in the focal region lay the groundwork for a broad spectrum of research endeavors, with particular attention to their roles in light-atom interactions [29].

. The spin-orbit interaction in the focal plane of tightly focused LG beams significantly influences the transversal and longitudinal electromagnetic field components associated with conical wavevector structure. The longitudinal field holds vast potential applications including particle accelerators [30], laser ablation [31], nonlinear optics [32], confocal laser scanning microscopy [33,34], and Raman spectroscopy [35]. Extensive research has been conducted on techniques aimed at detecting the longitudinal field [36,37], underscoring the growing interest and recognition of its importance across diverse scientific disciplines.

In this paper, the localized quadrupole excitation of an atom in the central region of tightly focused LG beams, taking into account the spin-orbit interaction (for LG beams with parallel and antiparallel SAM and OAM) in the nonparaxial limit has been investigated. The quadrupole Rabi frequency, as a crucial parameter, is calculated for the allowed quadrupole transition channels. Additionally, the impact of strong focusing on the excitation probability at different transversal positions of the atom relative to the central axis is explored.

2. Intensity distribution of tightly focused LB beams in nonparaxial limit

To analyse the intensity distribution of tightly focused LG beams in nonparaxial limit and facilitate subsequent discussions on light-atom interaction, it is helpful to represent the LG beams as a superposition of partial plane waves incident on a high numerical aperture (NA) focusing lens. Considering the electric fields as a complete set of orthogonal modes in cylindrical coordinates and under the assumption of negligible depolarization in homogeneous focusing medium, the electric field distribution in the focal plane using the Debye-Wolf diffraction integral can be described as [38]:

$$\boldsymbol{E}_f(\boldsymbol{R}) = -\frac{ikf}{2\pi}\int_0^{\theta_0}\int_0^{2\pi} \sin\theta_k \sqrt{\cos\theta_k} E_{lp}(\theta_k, \phi_k) \left[\widehat{M}(\theta_k, \phi_k)\boldsymbol{e}\right] e^{i\boldsymbol{k}\cdot\boldsymbol{R}} d\theta_k d\phi_k \tag{1}$$

where $\widehat{M}(\theta_k, \phi_k)$ is transformation matrix converting the input polarization, **e,** to the polarization in the focal region, $\boldsymbol{e}_f$, $\boldsymbol{k} = k\sin\theta_k\cos\phi_k\boldsymbol{e}_x + k\sin\theta_k\sin\phi_k\boldsymbol{e}_y + k\cos\theta_k\boldsymbol{e}_z$ is wavevector of the partial plane waves, with $k = 2\pi/\lambda$, where λ is the wavelength. $E_{lp}(\theta_k, \phi_k)$ represents the distribution of amplitude in **k**-space on the reference sphere, s, with focal radius, f (Fig. (1)). The knowledge of

Optics EXPRESS

$E_{lp}(\theta_k, \phi_k)$ is sufficient to reconstruct the electric field of the beam in the focal region. Here, ϕ_k is the azimuthal angle, $\theta_k = \arctan \frac{k_\perp}{k_z}$ varies from 0 to θ_0, presents the diffraction angle of each diffracted ray, where $\theta_0 = arcsin(NA/\mu)$ is the maximum angle between the focused beam and the optical axis, with μ as the refractive index of the medium. The term of $\sqrt{\cos\theta_k}$ originates from the conservation of the energy flow on the reference sphere. The focusing system supposed to have rotational symmetry with respect to the optical axis, ensuring the lens is aplanatic and aberrationless to make a geometric transformation of the angular momentum.

The wavevector, **k**, after focusing under the geometric transformation, experiences a pure meridional rotation by the angle θ_k (Fig. (1)), accompanied by the rotation of the local polarization vectors **e.** In the geometric transformation, the unitary matrix $\widehat{M}(\theta_k, \phi_k)$ is given by:

$$\begin{aligned}\hat{M}(\theta_k, \phi_k) &= \hat{V}^\dagger \hat{R}_z(-\phi_k)\hat{R}_y(-\theta_k)\hat{R}_z(\phi_k)\hat{V} \\ &= \begin{pmatrix} \cos^2\frac{\theta_k}{2} & -\sin^2\frac{\theta_k}{2}e^{-2i\phi_k} & \sqrt{\frac{1}{2}}\sin\theta_k e^{-i\phi_k} \\ -\sin^2\frac{\theta_k}{2}e^{2i\phi_k} & \cos^2\frac{\theta_k}{2} & \sqrt{\frac{1}{2}}\sin\theta_k e^{i\phi_k} \\ -\sqrt{\frac{1}{2}}\sin\theta_k e^{i\phi_k} & -\sqrt{\frac{1}{2}}\sin\theta_k e^{-i\phi_k} & \cos^2\frac{\theta_k}{2} - \sin^2\frac{\theta_k}{2} \end{pmatrix}\end{aligned} \tag{2}$$

where $\widehat{R}_\alpha(\beta)$ is rotational matrix about α-axis by angle β, and $\widehat{V} = \frac{1}{\sqrt{2}}\begin{pmatrix} 1 & 1 & 0 \\ i & -i & 0 \\ 0 & 0 & \sqrt{2} \end{pmatrix}$ is the transformation matrix to circular basis ($\mathbf{e_+}$, $\mathbf{e_-}$, $\mathbf{e_z}$). This pure geometric transformation includes the spin-redirection geometric phase and results in a SAM to OAM conversion [28].

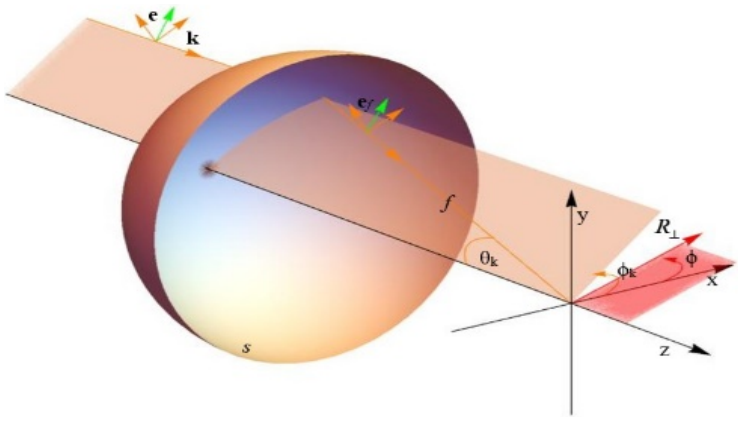

Fig. 1. Geometrical representation of the aplanatic focusing system. **R** is position vector of observation point in the focal region of the lens, **k** is vector describing the direction of a geometrical ray, and ***e*** and $\boldsymbol{e}_f$ are the polarization vector before and after focusing, respectively.

For an incident LG beam, the amplitude distribution at the entrance pupil of the focusing lens can be written as:

$$E_{lp}(\theta_k, \phi_k) = E_0 F_{lp}(\theta_k) e^{il\phi_k}, \tag{3}$$

where

$$F_{lp}(\theta_k) = \left(\sqrt{2}b_0\frac{\sin\theta_k}{\sin\theta_0}\right)^{|l|} e^{-\left(b_0\frac{\sin\theta_k}{\sin\theta_0}\right)^2} L_p^l\left(2\left(b_0\frac{\sin\theta_k}{\sin\theta_0}\right)^2\right), \tag{4}$$

Optics EXPRESS

with $b_0 = \frac{f \sin\theta_0}{w_0}$ as the filling factor, the ratio of the pupil radius to the beam waist w_0, l is the azimuthal mode index for the spiral phase shift, giving rise to an OAM of $l\hbar$ per photon, p presents the radial mode index and $L_p^{|\ell|}$ are the Laguerre polynomials. The electric field amplitude, $\mathsf{E}_{0,}$ is connected to the laser intensity via $E_0 = \sqrt{\frac{2\mu I}{c\varepsilon_0}}$, where c and ε_0 are the speed of light and vacuum permittivity, respectively. Substituting Eqs. (2) and (3) in Eq. (1),using $\boldsymbol{k}\cdot\boldsymbol{r} = \mathrm{kR}(\sin\theta_k \sin\theta\cos(\phi_k - \phi) + \cos\theta_k\cos\theta)$ and the integral representation of the Bessel function [39], $\int_0^{2\pi} d\phi_k \cos n\phi_k e^{i\rho\cos(\phi_k-\phi)} = 2\pi i^n J_n(\rho)\cos n\phi$, where J_n are Bessel functions of the first kind of order n, the electric field of the tightly focused LG beams in the circular basis reads:

$$\begin{aligned}\boldsymbol{E}_f(\boldsymbol{R}) = -i^{l+n+1}E_{0f}\int_0^{\theta_0} e^{i\bar{Z}\frac{\cos\theta_k}{\sin\theta_0}}\,(e^{il\phi}T_0^l(\bar{R}_\perp,\theta_k)\boldsymbol{e}_\sigma + T_{2\sigma}^l(\bar{R}_\perp,\theta_k)e^{i(l+2\sigma)\phi}\boldsymbol{e}_{-\sigma}\\ + T_\sigma^l(\bar{R}_\perp,\theta_k)e^{i(l+\sigma)\phi}\boldsymbol{e}_z)\sin\theta_k d\theta_k,\end{aligned} \tag{5}$$

where $E_{0f} = kfE_0$, and

$$T_n^l(\bar{R}_\perp,\theta_k) = \sqrt{\cos\theta_k}F_{lp}(\theta_k)\eta_n(\theta_k)J_{l+n}\left(\bar{R}_\perp\frac{\sin\theta_k}{\sin\theta_0}\right), \tag{6}$$

with $\bar{R}_\perp = kR_\perp\sin\theta_0$ and $\bar{Z} = kZ\sin\theta_0$, as size parameters, $n = \{0,\sigma,2\sigma\}$, $\eta_0(\theta_k) = \cos^2\frac{\theta_k}{2}$, $\eta_{2\sigma}(\theta_k) = -\sin^2\frac{\theta_k}{2}$, and $\eta_\sigma(\theta_k) = -\sin\theta_k$, where $\sigma = \pm 1$ is spin quantum number.

According Eq. (5), unlike the paraxial limit, the nonparaxial condition exhibits a significant interplay between polarization and the spatial dependence of the field, resulting to the polarization dependent OAM σ. The meticulous design of both SAM and OAM of the input beam serves as the foundation for controlling all three components of the field in the focal plane [40,41].

To comprehend the interaction between a localized atom and a tightly focused LG beam, while taking into account the aforementioned characteristics, we first examine the intensity distribution of the LG beam with both parallel and antiparallel SAM and OAM. As depicted in Fig. 2(a), the tightly focused LG beam with parallel SAM and OAM exhibits distinct features in its transversal, longitudinal, and total intensity distributions. Notably, it forms bright rings with respective size parameters $\bar{R}_\perp \approx 2.39$, 3.69 and 2.56 corresponding to respective radii of $R_\perp \approx 0.42\lambda$, 0.65λ, and 0.45λ. In contrast, Fig. 2(b) illustrates the behavior of the tightly focused LG beam with antiparallel OAM and SAM, where the constructive interference of optical rays results in a longitudinal intensity distribution in the central region. Comparing Figs. 2 (a) and 2(b), the longitudinal intensity, $\mathrm{I_z}$, for LG beam with antiparallel SAM and OAM is maximized at the focal center with a strength comparable to the transversal intensity. As the focusing angle, θ_0, increases the longitudinal intensity gradually intensifies, eventually surpassing the transversal intensity beyond $\theta_0 \geq 1.1$ rad or NA = 0.89 (Fig. (3)), and at $\theta_0 \approx 1.57$ rad (maximum NA), its ratio relative to the transversal intensity reaches a maximum of 1.59.

These findings emphasize that the combination of SAM and OAM of the tightly focused LG beam, as well as the degree of focusing, significantly influence the longitudinal component of the electric field. It is noticeable, despite LG beams with parallel and antiparallel SAM and OAM having the same intensity in the paraxial approximation, the intensity distribution of a tightly focused LG beam is highly sensitive to the spin-orbit interaction in nonparaxial conditions. The variation of SAM- and OAM-dependent intensity at sub-wavelength scales, perceptible to a trapped atom in the focal plane, modifies atomic transitions and unveils new phenomena that go beyond the paraxial description of atom-light interaction.

Optics EXPRESS

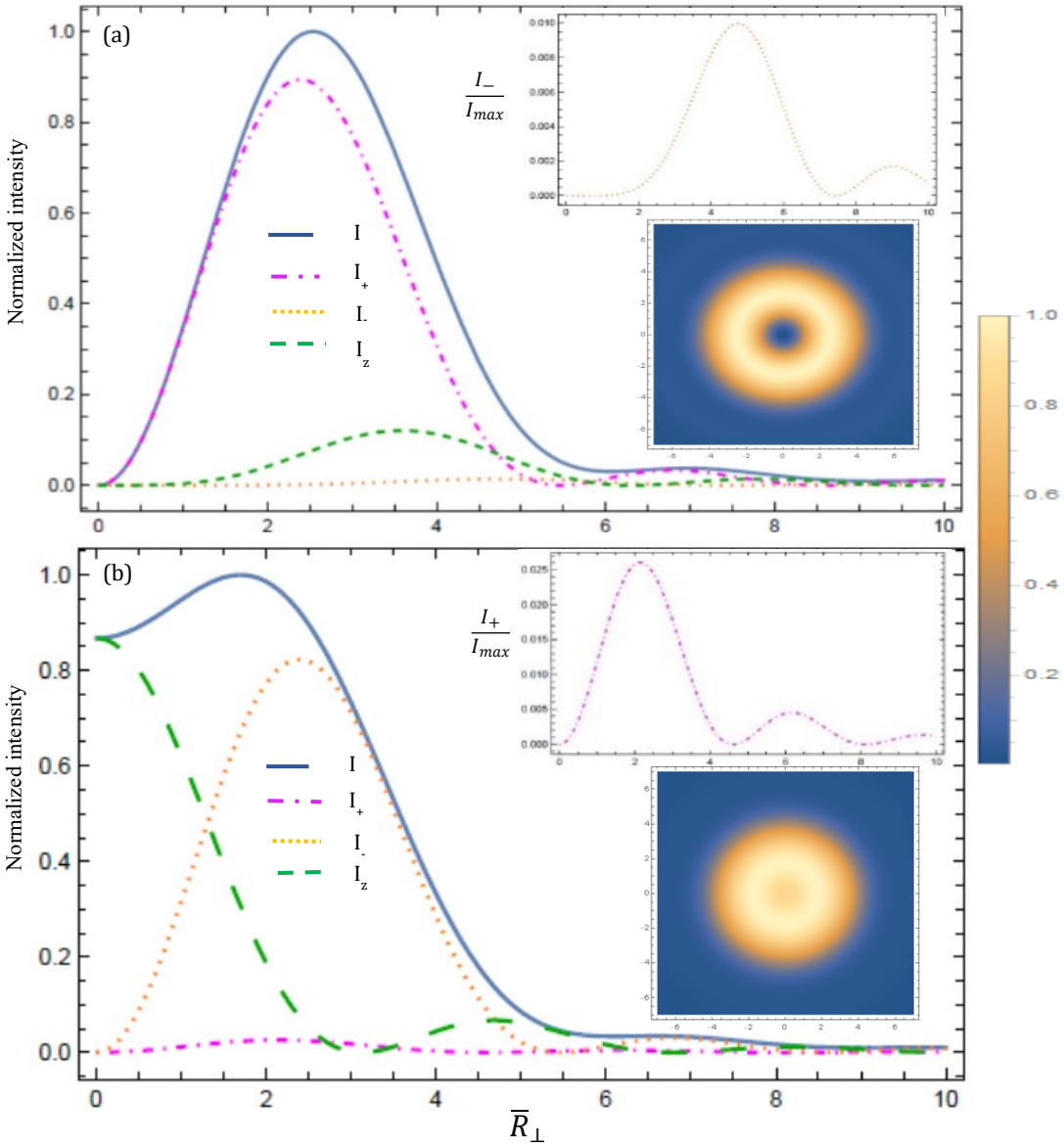

Fig. 2. The normalized intensity profile of right-circular-polarized, I_+ (dotdashed-magneta), left-circular-polarized, I_- (dotted-orange) and longitudinal, I_z (dashed-green) components and total intensity I (solid-blue) of LG beams with (a) parallel SAM and OAM ($l = 1,\ \sigma = 1$), and (b) antiparallel SAM and OAM($l = 1,\ \sigma = -1$) at the focusing plane under the tight focusing condition, $\theta_0 = 0.36\pi$ and $b_0 = 1$ versus the size parameter, $\bar{R}_\perp$. All values are normalized to the maximum value of total intensity I. The insets show magnified I_+/I_{max} and $I_-//I_{max}$ versus $\bar{R}_\perp$. The 3D density plots in the inset are total intensity at the focal plane.

Optics EXPRESS

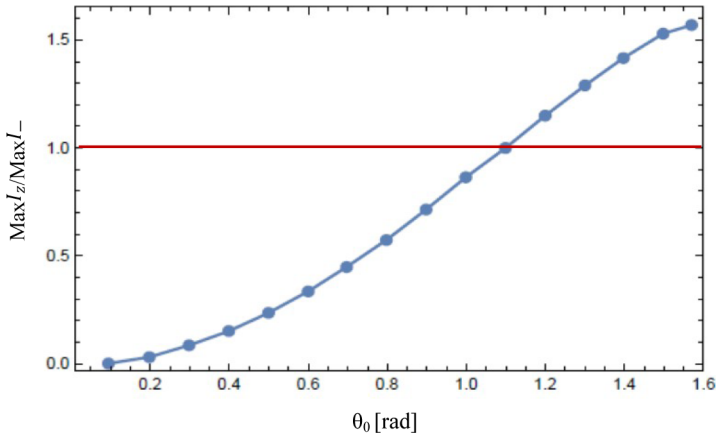

Fig. 3. The ratio of the maximum intensities of the longitudinal, I_z and left-circular-polarized component, I_- versus focusing angle θ_0 for LG beam with antiparallel SAM and OAM. Beyond the red line at the angle of 1.1 rad, the longitudinal component of electric field becomes higher than the transversal one.

3. Quadrupole excitation of a localized atom with tightly focused LG beams

In this section, a detailed theory is developed for quadrupole transition of a localized atom, trapped in the focal plane of a tightly focused LG beam with parallel and antiparallel SAM and OAM (Fig. 4), under general nonparaxial conditions. Given the significance of the Rabi frequency as a crucial experimental parameter in laser excitation and its utility as a primary means for directly controlling coherent light-atom interactions, the quadrupole Rabi frequency for such transition is presented.

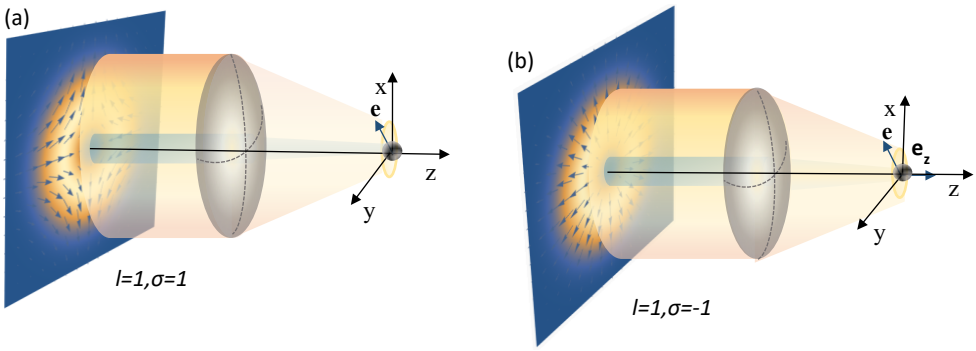

Fig. 4. Vector plot and intensity profile of LG beam with (a) parallel and (b) antiparallel SAM and OAM, along with schematic of the polarization vector of electric fields at the focal plane. The atom trapped in the central region of the tightly focused LG beam with parallel SAM and OAM experiences only transversal intensity variations. In contrast, at the center of the LG beam with antiparallel SAM and OAM components, the region is not completely dark due to the presence of a non-zero longitudinal electric field. As a result, the atom is exposed to both transversal and longitudinal intensity variations.

Here it should be considered that the design of large numerical aperture lenses for atom excitation employing tightly focused beams for experimental purposes necessitates careful consideration of the ultrahigh vacuum environment of atom traps. [42]. Moreover, to ensure that

Optics EXPRESS

the longitudinal and transversal field gradients discussed in section 2 being perceptible to the atom, it is assumed that the atom has been laser cooled to microkelvin temperatures [43].

Neglecting the electron's mass compared to that of the atom, the interaction Hamiltonian based on Power–Zienau–Woolley (PZW) picture can be given by [14,44]:

$$\widehat{H}_{int} = -e\boldsymbol{r}.\int_0^1 ds\boldsymbol{E}(\boldsymbol{R}+s\boldsymbol{r}), \tag{7}$$

where E is the electric field of the excitation laser beam with $\boldsymbol{R}(R_\perp,\phi,Z)$ and $\boldsymbol{r}(r_\perp,\varphi,z)$ as the centre of mass and internal coordinates in the focus, respectively. Using Eqs. (5) and (7) and considering the quantization axis along the z-direction, the interaction Hamiltonian can be written as:

$$\begin{aligned}\widehat{H}_{\rm int} = i^{l+n+1}eE_{0f}r\cdot\int_0^1\int_0^{\theta_0}\{T_0^l(|\bar{\boldsymbol{R}}_\perp+s\bar{\boldsymbol{r}}_\perp|,\theta_k)e^{il\phi_R}\boldsymbol{e}_\sigma + T_{2\sigma}^l(|\bar{\boldsymbol{R}}_\perp+s\bar{\boldsymbol{r}}_\perp|,\theta_k)e^{i(l+2\sigma)\phi_R}\boldsymbol{e}_{-\sigma}\\ + T_\sigma^l(|\bar{\boldsymbol{R}}_\perp+s\bar{\boldsymbol{r}}|_\perp,\theta_k)e^{i(l+\sigma)\phi_R}\boldsymbol{e}_z\}\times e^{i(\bar{Z}+s\bar{z})\frac{\cos\theta_k}{\sin\theta_0}}\sin\theta_k d\theta_k ds\end{aligned} \tag{8}$$

where ϕ_R is the azimuthal angle of the vector $\widehat{\boldsymbol{R}}_\perp+s\bar{\boldsymbol{r}}_\perp$ [14]. By Taylor expansion around $\bar{R}_\perp$ and doing some straightforward calculations, one can drive:

$$T_n^l\left(|\bar{\boldsymbol{R}}_\perp+s\bar{\boldsymbol{r}}_\perp|,q_k\right)e^{i(l+n)\phi_R}\approx T_m^l\left(\bar{R}_\perp,\theta_k\right)e^{i(l+n)\phi}+s\bar{r}_\perp T_m^{l+}\left(\bar{R}_\perp,\theta_k\right)e^{i\varphi}e^{i(l+n-1)\phi}+s\bar{r}_\perp T_n^l-\left(\bar{R}_\perp,\theta_k\right)e^{-i\varphi}e^{i(l+n+1)\phi} \tag{9}$$

where

$$T_n^{l+}(\bar{R}_\perp,\theta_k)=\frac{1}{2}\left(\frac{dT_n^l(\bar{R}_\perp,\theta_k)}{d\bar{R}_\perp}+(n+l)\frac{T_n^l(\bar{R}_\perp,\theta_k)}{\bar{R}_\perp}\right), \tag{10}$$

$$T_n^{l-}(\bar{R}_\perp,\theta_k)=\frac{1}{2}\left(\frac{dT_n^l(\bar{R}_\perp,\theta_k)}{d\bar{R}_\perp}-(n+l)\frac{T_n^l(\bar{R}_\perp,\theta_k)}{\bar{R}_\perp}\right). \tag{11}$$

Using the notation $\langle f\rangle=\int_0^{\theta_0} f\sin\theta_k d\theta_k$, substituting $e^{i(\bar{Z}+s\bar{z})\frac{\cos\theta_k}{\sin\theta_0}}\approx e^{i(\bar{Z})\frac{\cos\theta_k}{\sin\theta_0}}\left(1+i\bar{z}s\frac{\cos\theta_k}{\sin\theta_0}\right)$, and integrating Eq. (8) over s, the interaction Hamiltonian in the focal plane $\bar{Z}=0$ is given by:

$$H_{\rm int}=H_{\rm int}^d+H_{\rm int}^{qt+}+H_{\rm int}^{qt-}+H_{\rm int}^{qz} \tag{12}$$

In Eq. (12), the first expression,

$$H_{\rm int}^d=-\frac{i^{l+n+3}}{2}eE_{0f}\mathbf{r}\cdot\left(\left\langle T_0^l\right\rangle e^{il\phi}\mathbf{e}_\sigma+\left\langle T_{2\sigma}^l\right\rangle e^{i(l+2\sigma)\phi}\mathbf{e}_{-\sigma}+\left\langle T_\sigma^l\right\rangle e^{i(l+\sigma)\phi}\mathbf{e}_z\right), \tag{13}$$

constructed from the sum of the terms linear in the components of the internal vector, r, represents the dipole interaction Hamiltonian. The other expressions,

$$H_{\rm int}^{qt+}=-\frac{i^{l+n+3}}{2}eE_{0f}e^{i\varphi}e^{-i\phi}\bar{r}_\perp\mathbf{r}\cdot(\left\langle T_0^{l+}\right\rangle e^{il\phi}\mathbf{e}_\sigma+\left\langle T_{2\sigma}^{l+}\right\rangle e^{i(l+2\sigma)\phi}\mathbf{e}_{-\sigma}+\left\langle T_\sigma^{l+}\right\rangle e^{i(l+\sigma)\phi}\mathbf{e}_z), \tag{14}$$

$$H_{\rm int}^{qt-}=-\frac{i^{l+n+3}}{2}eE_{0f}e^{-i\varphi}e^{i\phi}\bar{r}_\perp\mathbf{r}\cdot(\left\langle T_0^{l-}\right\rangle e^{il\phi}\mathbf{e}_\sigma+\left\langle T_{2\sigma}^{l-}\right\rangle e^{i(l+2\sigma)\phi}\mathbf{e}_{-\sigma}+\left\langle T_\sigma^{l-}\right\rangle e^{i(l+\sigma)\phi}\mathbf{e}_z), \tag{15}$$

and

$$H_{\rm int}^{qz}=-\frac{i^{l+n+4}}{2}eE_{0f}\bar{z}\mathbf{r}\cdot(\left\langle\frac{\cos\theta_k}{\sin\theta_0}T_0^l\right\rangle e^{il\phi}\mathbf{e}_\sigma+\left\langle\frac{\cos\theta_k}{\sin\theta_0}T_{2\sigma}^l\right\rangle e^{i(l+2\sigma)\phi}\mathbf{e}_{-\sigma}+\left\langle\frac{\cos\theta_k}{\sin\theta_0}T_\sigma^l\right\rangle e^{i(l+\sigma)\phi}\mathbf{e}_z), \tag{16}$$

with quadratic internal components, serve as the respective transversal and longitudinal quadrupole interaction Hamiltonians. The second and third terms of Eqs. (13)-(16) emerge from the tightly

Optics EXPRESS

focusing nonparaxial condition, demonstrating the transitions wherein the SAM of light can take part in the centre of mass motion due to the spin-orbit interaction.

In order to determine the interaction strength of each transition, we consider an atom with an outer electron confined within the dark (dim) central region of the LG beam with parallel (antiparallel) SAM and OAM (Fig. (5)). The atom can then be driven from an initial state, $|n_i, j_i, m_i\rangle$ to a final state, $|n_f, j_f, m_f\rangle$, specified by nα, jα and mα as quantum numbers, associated with the principle quantum number, the total-, and z-component of the state's angular momentum, α, respectively. Moreover, it is assumed that the frequency of the tightly focused LG beam is tunable to the different magnetic sublevels of the excited state and the lifetime of the excited state is long enough that the spontaneous emission from these levels is negligible. Additionally, to allow probing all the transition channels in such intensity distribution landscape, the hyperfine structure of the atom is neglected and only magnetic Zeeman-split levels in a static magnetic field (z-direction) are considered. Subsequently, the transitions can be determined by the total angular momentum as: (i) dipole transitions, in which SAM can be transferred between the electromagnetic field and the internal state of the atom while the exchange of OAM occurs only between the light and the atom's center of mass motion [45], and (ii) quadrupole transitions, where the interaction can also involve the transfer of OAM to the internal motion of the atom [13,14].

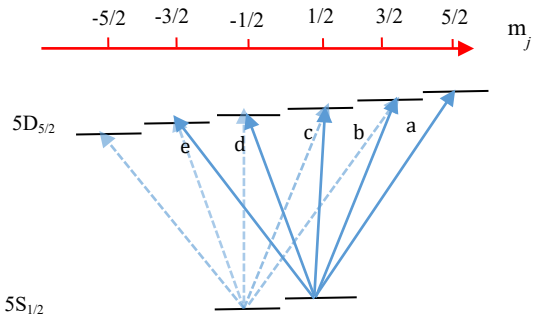

Fig. 5. The energy level diagram of quadrupole transition $5S \rightarrow 5D$ of a cold Rubidium atom, ^{87}Rb. The quadrupole transitions Δm = 2,1, 0 -1 and -2 are labled from a to e.

Building upon the theoretical framework outlined above for the interaction strength of various transitions driven by a tightly focused LG beam with parallel (antiparallel) SAM and OAM, we now turn our attention to the Rabi frequencies associated with quadrupole transitions. The Rabi frequency, $\Omega_p^{\Delta m}$ ($\Omega_{ap}^{\Delta m}$) of different channels of quadrupole transitions, $j_f - j_i = 2$, are presented in Table (1), where $\Delta m = m_f - m_i$ is the angular momentum transfer in z-direction. The transition channels with $\Delta m = \pm 2$ are influenced by pure transversal intensity variations, whereas the other channels with $\Delta m = 0, \pm 1$ are influenced by both transversal and longitudinal intensity variation. Within the various transition channels, it is anticipated that Rabi frequencies Ω_p^2 and Ω_{ap}^0 of respective quadrupole transitions $\Delta m = 2$ and $\Delta m = 0$ are dominant in the central region of the focus. It is due to the sharp transversal variation of the intensity, I_+ (I_-) of the LG beam with parallel (antiparallel) SAM and OAM focused to a sub-wavelength radius (Figs. 2(a) and 2(b)), visible to the trapped atom in this region. In the dark central region of the focused LG beam with parallel SAM and OAM only the variations of I_+ contributes to the transition. In contrast, within the dim central region of the focused LG beam with antiparallel SAM and OAM, the additional longitudinal intensity variation is also considerable (Fig. 2(b)) and contributes to the quadrupole transition with Δm = 0.

Optics EXPRESS

Table 1. The quadrupole Rabi frequency, $\Omega_p^{\Delta m}$, and $\Omega_{ap}^{\Delta m}$ for the tightly focused LG beam with respective parallel and antiparallel SAM and OAM for different transition channels

$l=1$	σ=1	σ=-1
$\Delta m=0$	$\frac{1}{2\hbar}ekE_f \sin\theta_0(\langle f\vert r_\perp \mathbf{r}\cdot\mathbf{e}_+ e^{-i\varphi}\vert i\rangle \langle T_0^{1-}(\bar{R}_\perp,\theta_k)\rangle$ - $\langle f\vert r_\perp \mathbf{r}\cdot\mathbf{e}_- e^{i\varphi}\vert i\rangle \langle T_2^{1+}(\bar{R}_\perp,\theta_k)\rangle$ - $\langle f\vert z\mathbf{r}\cdot\mathbf{e}_z\vert i\rangle \left\langle T_1^1(\bar{R}_\perp,\theta_k)\frac{\cos\theta_k}{\sin\theta_0}\right\rangle)e^{2i\phi}$	$\frac{-1}{2\hbar}ekE_f \sin\theta_0(-\langle f\vert r_\perp \mathbf{r}\cdot\mathbf{e}_- e^{i\varphi}\vert i\rangle \langle T_0^{1+}(\bar{R}_\perp,\theta_k)\rangle$ + $\langle f\vert r_\perp \mathbf{r}\cdot\mathbf{e}_+ e^{-i\varphi}\vert i\rangle \langle T_{-2}^{1-}(\bar{R}_\perp,\theta_k)\rangle$ - $\langle f\vert z\mathbf{r}\cdot\mathbf{e}_z\vert i\rangle \left\langle T_{-1}^1(\bar{R}_\perp,\theta_k)\frac{\cos\theta_k}{\sin\theta_0}\right\rangle)$
$\Delta m=1$	$\frac{i}{2\hbar}ekE_f \sin\theta_0(\langle f\vert r_\perp \mathbf{r}\cdot\mathbf{e}_z e^{i\varphi}\vert i\rangle \langle T_1^{1+}(\bar{R}_\perp,\theta_k)\rangle$ + $\langle f\vert rz\mathbf{r}\cdot\mathbf{e}_+\vert i\rangle \left\langle T_0^1(\bar{R}_\perp,\theta_k)\frac{\cos\theta_k}{\sin\theta_0}\right\rangle)e^{i\phi}$	$\frac{-i}{2\hbar}ekE_f \sin\theta_0(\langle f\vert r_\perp \mathbf{r}\cdot\mathbf{e}_z e^{i\varphi}\vert i\rangle \langle T_{-1}^{1+}(\bar{R}_\perp,\theta_k)\rangle$ + $\langle f\vert z\mathbf{r}\cdot\mathbf{e}_+\vert i\rangle \left\langle T_{-2}^1(\bar{R}_\perp,\theta_k)\frac{\cos\theta_k}{\sin\theta_0}\right\rangle)e^{-i\phi}$
$\Delta m=2$	$\frac{1}{2\hbar}ekE_f \sin\theta_0 \langle f\vert r_\perp \mathbf{r}\cdot\mathbf{e}_+ e^{i\varphi}\vert i\rangle \langle T_0^{1+}(\bar{R}_\perp,\theta_k)\rangle$	$\frac{-1}{2\hbar}ekE_f \sin\theta_0 \langle f\vert r_\perp \mathbf{r}\cdot\mathbf{e}_+ e^{i\varphi}\vert i\rangle \langle T_{-2}^{1+}(\bar{R}_\perp,\theta_k)\rangle e^{-2i\phi}$
$\Delta m=-1$	$\frac{i}{2\hbar}ekE_f \sin\theta_0(\langle f\vert r_\perp \mathbf{r}\cdot\mathbf{e}_z e^{-i\varphi}\vert i\rangle \langle T_1^{1-}(\bar{R}_\perp,\theta_k)\rangle$ - $\langle f\vert z\mathbf{r}\cdot\mathbf{e}_-\vert i\rangle \left\langle T_2^1(\bar{R}_\perp,\theta_k)\frac{\cos\theta_k}{\sin\theta_0}\right\rangle)e^{3i\phi}$	$\frac{-i}{2\hbar}ekE_f \sin\theta_0(\langle f\vert r_\perp \mathbf{r}\cdot e_z\mathbf{e}^{-i\varphi}\vert i\rangle \langle T_{-1}^{-1}(\bar{R}_\perp,\theta_k)\rangle$ - $\langle f\vert z\mathbf{r}\cdot\mathbf{e}_-\vert i\rangle \left\langle T_0^1(\bar{R}_\perp,\theta_k)\frac{\cos\theta_k}{\sin\theta_0}\right\rangle)e^{i\phi}$
$\Delta m=-2$	$\frac{-1}{2\hbar}ekE_f \sin\theta_0 \langle f\vert r_\perp \mathbf{r}\cdot\mathbf{e}_- e^{-i\varphi}\vert i\rangle \langle T_2^{1-}(\bar{R}_\perp,\theta_k)\rangle e^{4i\phi}$	$\frac{1}{2\hbar}ekE_f \sin\theta_0 \langle f\vert r_\perp \mathbf{r}\cdot\mathbf{e}_- e^{-i\varphi}\vert i\rangle \langle T_0^{1-}(\bar{R}_\perp,\theta_k)\rangle e^{2i\phi}$

Using spherical tensors, $\psi_0^1 = \sqrt{\frac{3}{4\pi}}\cos\boldsymbol{\theta}$ and $\psi_1^{\pm1} = \mp\sqrt{\frac{3}{8\pi}}\sin\boldsymbol{\theta}\boldsymbol{e}^{\pm i\varphi}$ and converting the lower ranks into the sum of the higher ones as:

$$\psi_1^1\psi_1^1 = \psi_2^2, \psi_0^1\psi_0^1 = \left(\sqrt{\tfrac{2}{3}}\psi_0^2 - \sqrt{\tfrac{1}{3}}\psi_0^0\right),\ \psi_1^{-1}\psi_1^1 = \sqrt{\tfrac{1}{6}}\psi_2^0 - \sqrt{\tfrac{1}{2}}\psi_1^0 + \sqrt{\tfrac{1}{3}}\psi_0^0,$$
$$\psi_1^1\psi_1^{-1} = \sqrt{\tfrac{1}{6}}\psi_2^0 + \sqrt{\tfrac{1}{2}}\psi_1^0 + \sqrt{\tfrac{1}{3}}\psi_0^0$$

and employing the Wigner-Ekart theorem, the quadrupole Rabi frequency of the dominant transitions for the atom trapped in the central region of a tightly focused LG beam with the respective antiparallel and parallel SAM and OAM can be written in terms of Clebsch-Gordan coefficients as:

$$\Omega_{ap}^0(\bar{R}_\perp,\theta_0) = \Omega_0\frac{\langle J_i m_i 20\vert J_f m_f\rangle}{\sqrt{3}}\left(\sqrt{2}\left\langle T_{-1}^1(\bar{R}_\perp,\theta_k)\frac{\cos\theta_k}{\sin\theta_0}\right\rangle - \left\langle T_0^{1+}(\bar{R}_\perp,\theta_k)\right\rangle + \left\langle T_{-2}^{1-}(\bar{R}_\perp,\theta_k)\right\rangle\right), \tag{17}$$

and

$$\Omega_p^2\left(\bar{R}_\perp,\theta_0\right) = \Omega_0\ \langle J_i m_i 22\vert\ J_f m_f\rangle\left\langle T_0^{1+}\left(\bar{R}_\perp,\theta_k\right)\right\rangle \tag{18}$$

In the above equations, $\Omega_0 = \sqrt{\frac{8\pi^2e^2I}{9c\varepsilon_0\hbar^2}}k^2 f\sin\theta_0\langle n_f J_f\left\|r^2\right\|n_i J_i\rangle$ represents the maximum quadrupole Rabi frequency induced by a tightly focused LG beam. The Clebsch Gordan coefficients express the relative orientation between the excitation electric field at the focus and quadrupole moment of the atom when it exists in a superposition of states.

As an illustrative example, let's consider a trapped Rubidium atom, specifically ^{87}Rb, initially in the ground state, $\vert 5S_{1/2}, J_i = 1/2, m_i = 1/2\rangle$, which can be excited through quadrupole transitions labeled as a, b, c, d and e (Fig. (5)). The quadrupole Rabi frequencies profile of the transition channels are depicted in Fig. (6) for a trapped ^{87}Rb excited with a tightly focused LG beam considering focusing parameters $\theta_0 = 0.36\pi$ and $b_0 = 1$. The population distribution among the Zeeman levels of the excited state is strongly influenced by the atom's position relative to the center of the focused LG beam. As shown in left column of Fig. (6) for the LG beam with parallel SAM and OAM, by transversally positioning the atom at radii of $0.51\lambda, 0.67\lambda, 0.86\lambda$, and 1.1λ from the center, the intensity gradients across the focusing plane induce different quadrupole transitions $\Delta m = 1,\ 0, -1, -2$ with probabilities of 10%, 10%, 2%, 0.1% relative to the maximum value of Ω_p^2 . Conversely, when the atom is trapped within the dim region of the LG beam with antiparallel SAM and OAM, it undergoes a quadrupole transition, $\Delta m = 0$ with a probability of 58% relative to Ω_P^2. This transition arises due to the effects of both longitudinal

Optics EXPRESS

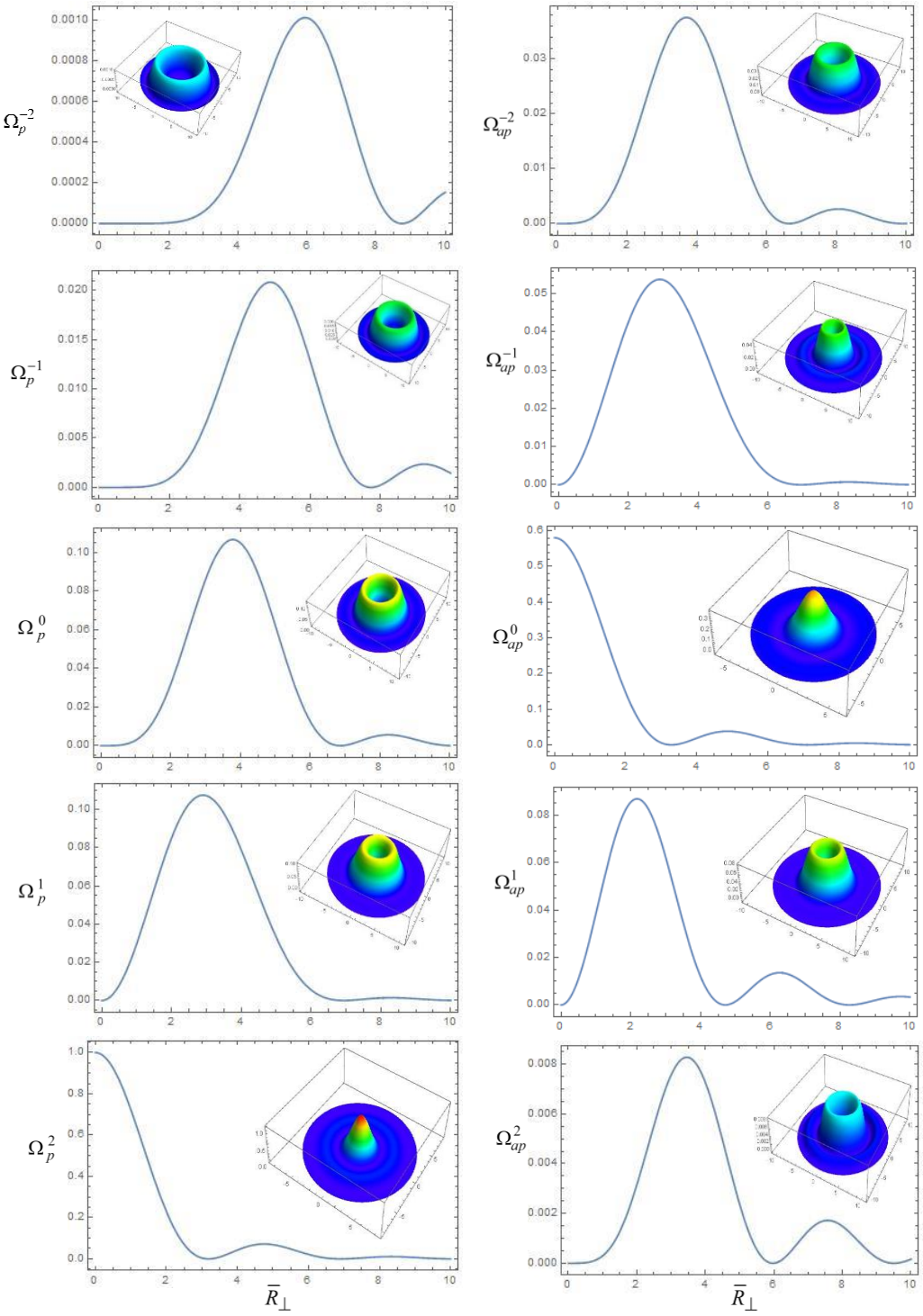

Fig. 6. The quadrupole Rabi frequency profile of a trapped ^{87}Rb excited with a tightly focused LG beam with parallel (left column) and antiparallel (right column) SAM and OAM for different transition channels as a function of size parameter, $\bar{R}_\perp$ for different angular momentum transfer $\Delta m = -2,\ -1,\ 0,\ 1,\ 2$. The data are normalized to the maximum value of Ω_P^2 for the tightly focused condition $\theta_0 = 0.36\pi$ and $b_0 = 1$.

Optics EXPRESS

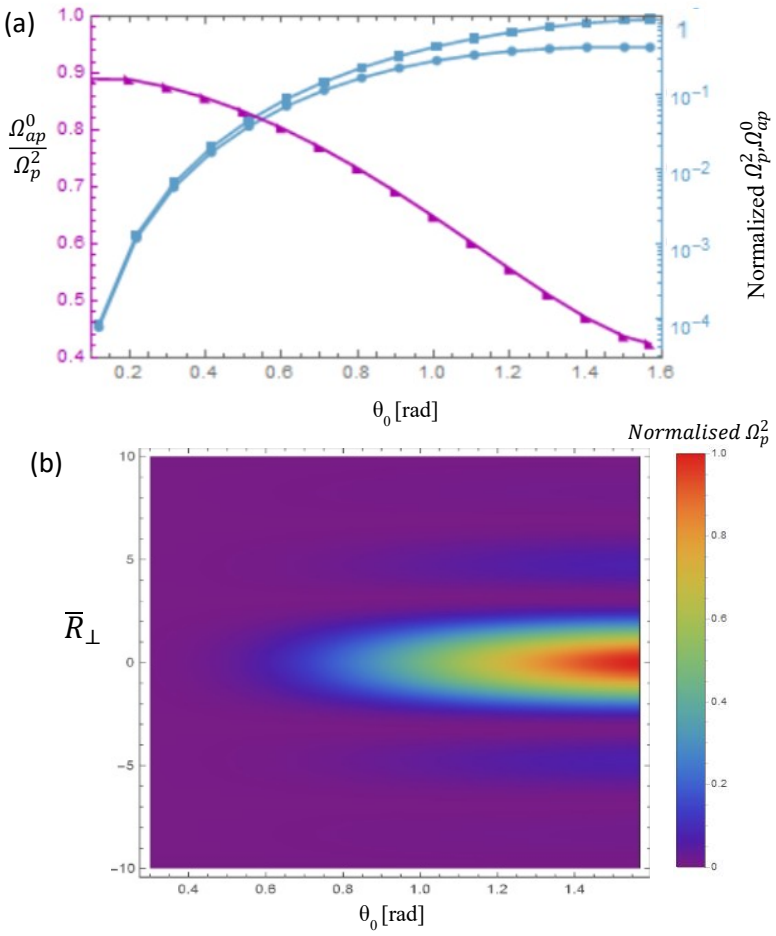

Fig. 7. (a) Peak values of Ω_p^2 (blue-rectangle) and Ω_{ap}^0 (blue-circle) normalized to maximum value of Ω_p^2, and Ω_{ap}^0/Ω_p^2 (magenta-triangle) versus θ_0 . (b) The normalized quadrupole Rabi frequency, Ω_p^2 within the focal plane versus θ_0 and the transversal position of atom.

and transversal electric field variations which can be altered by tunning focusing parameters. Furthermore, coherent transverse displacement of the atom from the beam center results in additional transitions $\Delta m = 2, 1, -1, -2$ at positions $R_\perp \approx 0.61\lambda,\ 0.39\lambda, 0.47\lambda$ and, 0.67λ with respective probabilities of approximately 0.8%, 8.3%, 5.4%, and 3.7% relative to Ω_P^2. The lateral displacement of atom away from the center and transfer of orbital angular momentum to the center of mass due to spin-orbit interaction, induces rotational motion of atom around the z-axis coupled to the excited state. Interestingly, the profile distribution of Ω_P^2 and Ω_{ap}^0 are similar with the radius of $R_\perp \approx 0.3\lambda$ (Fig. (6)) due to the transversal distribution of intensity at the focal plane Z = 0.

In a practical aspect, increasing the quadrupole transition probability in the central region of tightly focused LG beams enhances the signal-to-noise ratio in atom detection and facilitates the selective quadrupole excitation of atoms. It is worth noting that achieving high-fidelity quadrupole Rabi frequencies requires precise control over the field strength at the focus. Even minor intensity fluctuations can lead to unwanted heating of the atom, degrading the fidelity of

Optics EXPRESS

the transitions [46]. Additionally, to maintain the fidelity, stringent control over the OAM and SAM purity of the tightly focused excitation beam is essential.

To examine the influence of the focussing parameters, Fig. (7) illustrates the dependence of the quadrupole excitation Rabi frequency of the atom trapped in the central region of the focused LG beam with a parallel (antiparallel) SAM and OAM as a function of the focusing angle, θ_0. As shown in Fig. 7(a), the Rabi frequency exhibits a rapid increase with the growth of focusing angle. The peak values of Ω^0_{ap} reaches maximum at $\theta_0 \approx 1.1$ rad, while Ω^2_p continues to grow. Beyond this point, further increments in the focusing angle yield only marginal changes in the Rabi frequency Ω^0_{ap}, resulting in no significant enhancement in transition strength. On the other hand, the ratio between Ω^0_{ap} and Ω^2_p exhibits a decreasing trend with increasing focusing angle, reducing from approximately 90% at $\theta_0 = 0.1$ rad to about 42% at the maximum focusing angle of $\theta_0 = 1.57$ rad. The reduction can be ascribed to the longitudinal intensity variations that manifest near the center of the LG beam with antiparallel SAM and OAM. Figure 7(b) illustrates the transversal position where atom undergoes quadrupole transition under the influence of the LG beam with parallel SAM and OAM, demonstrating its correlation with the focusing angle. This observation provides valuable insights into the preferred range of focusing angles for optimizing the Rabi frequency and, consequently, the transition strength in the atom.

4. Conclusion

In this study, the quadrupole interaction of tightly focused LG beams with localized atoms, beyond the paraxial limit in the focal region has been investigated. The study focused on a specific scenario involving polarized LG beams with parallel and antiparallel SAM and OAM. It is important to highlight that this analysis has broader applicability and can be extended to include beams with more complex structures.

The results demonstrate the remarkable sensitivity of quadrupole excitation probability to the combined choice of SAM and OAM in the tightly focused LG beam, arising from the spin-orbit interaction in the focal plane. The sharp polarization-dependent intensity gradients in the vicinity of the focal plane leads to various quadrupole transition channels. Furthermore, the longitudinal polarization component plays the significant role in quadrupole transition when dealing with atoms trapped at the dim center of a focused LG beam with antiparallel SAM and OAM. The investigation has revealed that the Rabi frequency exhibits strong dependence on the focusing angle and grows by focusing strength. Rabi frequency Ω^2_p resulted from pure transversal intensity variation in the central region grows with the focusing angle while Ω^0_{ap} saturates beyond focusing angle 1.1 Rad because of existing longitudinal electric field in the center. This feature can serve as a control parameter, enabling precise adjustment of the transition probability strength when utilizing LG beams with parallel SAM and OAM, in contrast to those with antiparallel configuration. The localized atom within tightly focused LG beams including the transfer of orbital angular momentum modified by spin-orbit interactions, offers significant promise which paves the way for innovative techniques in quadrupole excitation of localized atoms, with applications extending to various fields such as storage, manipulation, and transfer of qudits.

The sub-wavelength size of the focus region ensures sharp intensity variations exclusively within the vicinity of the interacting atom, while neighboring atoms remaining unaffected by the field gradient. This feature renders the approach suitable for noise-free, high-fidelity qudit addressing—a crucial foundation for the development of scalable quantum logic devices. It opens up exciting possibilities for implementing quantum computers, offering a path towards significantly enhanced computational arrays with a high degree of integration and long-term stability [7,47].

Disclosures. The authors declare no conflicts of interest.

Optics EXPRESS

Data availability. Data underlying the results presented in this paper are not publicly available at this time but may be obtained from the authors upon reasonable request.

References

1. O. M. Maragò, O. M. Maragò, P. H. Jones, *et al.*, "Optical trapping and manipulation of nanostructures," Nat. Nanotechol. **8**(11), 807–819 (2013).
2. N. Schlosser, N. Reymond, N. Protsenko, *et al.*, "Sub-poissonian loading of single atoms in a microscopic dipole trap," Nature **411**(6841), 1024–1027 (2001).
3. F. Nogrette, H. Labuhn, S. Ravets, *et al.*, "Single-Atom Trapping in Holographic 2D Arrays of Microtraps with Arbitrary Geometries," Phys. Rev. X **4**(2), 021034 (2014).
4. J. Beugnon, C. Tuchendler, H. Marion, *et al.*, "Two-dimensional transport and transfer of a single atomic qubit in optical tweezers," Nat. Phys. **3**, 696–699 (2007).
5. A. W. Young, W. J. Eckner, and W. R. Milner, "Half-minute-scale atomic coherence and high relative stability in a tweezer clock," Nature **588**(7838), 408–413 (2020).
6. J. Wang and L. Liang, "Generation and detection of structured light: a review," Front. Phys. **9**, 688284 (2021).
7. D. Bluvstein, H. Levine, G. Semeghini, *et al.*, "A quantum processor based on coherent transport of entangled atom arrays," Nature **604**(7906), 451–456 (2022).
8. J. P. Covey, H. Weinfurter, and H. Bernien, "Quantum networks with neutral atom processing nodes," npj Quantum Inf. **9**(1), 90 (2023).
9. K. Wintersperger, F. Dommert, T. Ehmer, *et al.*, "Neutral atom quantum computing hardware: performance and end-user perspective," EPJ Quantum Technol. **10**(1), 32 (2023).
10. L. Henriet, L. Beguin, A. Signoles, *et al.*, "Quantum computing with neutral atoms," Quantum **4**, 327327 (2020).
11. V. E. Lembessis and M. Babiker, "Light-induced torque for the generation of persistent current flow in atomic gas BoseEinstein condensates," Phys. Rev. A **82**(5), 051402 (2010).
12. W. Schmiegelow, J. Schulz, H. Kaufmann, *et al.*, "Transfer of optical orbital angular momentum to a bound electron," Nat. Commun. **7**(1), 12998 (2016).
13. L. Mashhadi, "Three-photon Gaussian–Gaussian–Laguerre–Gaussian excitation of a localized atom to a highly excited Rydberg state," J. Phys. B: At. Mol. Opt. Phys. **50**(24), 245201 (2017).
14. L. Mashhadi, "Tightly trapped highly excited Rydberg atom in dipole-quadrupole potential landscape," J. Mod. Opt. **66**(17), 1725–1735 (2019).
15. A. Nicolas, L. Veissier, L. Giner, *et al.*, "A quantum memory for orbital angular momentum photonic qubits," Nat. Photonics **8**(3), 234–238 (2014).
16. P. Xu, X. He, J. Wang, *et al.*, "Trapping a single atom in a blue detuned optical bottle beam trap," Opt. Lett. **35**(13), 2164–2166 (2010).
17. A. Sharon, G. W. Kennedy, J. T. Biedermann, *et al.*, "Confinement of ultracold atoms in a Laguerre–Gaussian laser beam created with diffractive optics," Opt. Commun. **321**, 110–115 (2014).
18. M. Gambetta Jerry, M. Chow Jerry, and M. Steffen, "Building logical qubits in a superconducting quantum computing system," Quant. Inf. **3**, 1–7 (2017).
19. K. R. Brown, J. Chiaverini, J. M. Sage, *et al.*, "Materials challenges for trapped-ion quantum computers," Nat. Rev. Mat. **6**(10), 892–905 (2021).
20. G. F. Quinteiro, F. Schmidt-Kaler, and Christian T. Schmiegelow, "Schmiegelow 'Twisted-Light–Ion Interaction: The Role of Longitudinal Fields'," Phys. Rev. Lett. **119**(25), 253203 (2017).
21. S. Franke-Arnold, L. Allen, and M. Padgett, "Advances in optical angular momentum," Laser Photonics Rev. **2**(4), 299–313 (2008).
22. L. Allen and M. Padgett, "Twisted Photons," Wiley-VCH **2**, 1–12 (2011).
23. M. Babiker, C. R. Bennett, D. L. Andrews, *et al.*, "Orbital Angular Momentum Exchange in the Interaction of Twisted Light with Molecules," Phys. Rev. Lett. **89**(14), 143601 (2002).
24. Y. Wang, Z. Hu, S. C. Banders, *et al.*, "Qudits and HighDimensional Quantum Computing," Front. Phys. **8**, 589504 (2020).
25. Y. Chi, J. Huang, Z. Zhang, *et al.*, "A programmable qudit-based quantum processor," Nat. Commun. **13**(1), 1166 (2022).
26. M. Malik, M. Erhard, M. Huber, *et al.*, "Multi-photon entanglement in high dimensions," Nat. Photonics **10**(4), 248–252 (2016).
27. A. V. Arzola, L. Chvatal, and P. Zemanek, "Spin to orbital light momentum conversion visualized by particle trajectory," Sci. Rep. **9**(1), 4127 (2019).
28. K. Y. Bliokh, F. J. Rodriguez-Fortuno, and A. V. Zayats, "Spin–orbit interactions of light," Nat. Photonics **9**(12), 796–808 (2015).
29. J. Wang, F. Castellucci, and S. Franke-Arnold, "Vectorial light–matter interaction: Exploring spatially structured complex light fields," AVS Quantum Sci. **2**(3), 031702 (2020).
30. S. Carbajo, E. A. Nanni, L. Jie Wong, *et al.*, "Direct longitudinal laser acceleration of electrons in free space," Phys. Rev. Accel. Beams **19**(2), 021303 (2016).
31. Y. Kozawa, M. Sato, Y. Uesugi, *et al.*, "Laser microprocessing of metal surfaces using a tightly focused radially polarized beam," Opt. Lett. **45**(22), 6234–6237 (2020).

Optics EXPRESS

32. N. Poulvellarie, U. Dave, K. Alexander, *et al.*, "Second-harmonic generation enabled by longitudinal electric-field components in photonic wire waveguides," Phys. Rev. A **102**(2), 023521 (2020).
33. P. Meng, S. Pereira, and P. Urbach, "Confocal microscopy with a radially polarized focused beam," Opt. Express **26**(23), 29600 (2018).
34. N. Hayazawa, Y. Saito, and S. Kawata, "Detection and characterization of longitudinal field for tip-enhanced Raman spectroscopy," Appl. Phys. Lett. **85**(25), 6239–6241 (2004).
35. Y Kozawa and C Sato, Advanced Solid-State Photonics, "Enhanced Detection of Longitudinal Field of a Radially Polarized Beam in Confocal Laser Microscopy," OSA ISBN: 978-1-55752-968-8, STh3 K.2 (2011).
36. C. Ecoffey and T. Grosjean, "Far-field mapping of the longitudinal magnetic and electric optical fields," Opt. Lett. **38**(23), 4974 (2013).
37. L. Novotny, M. R. Beversluis, K. S. Youngworth, *et al.*, "Longitudinal Field Modes Probed by Single Molecules," Phys. Rev. Lett. **86**(23), 5251–5254 (2001).
38. B. Richards and E. Wolf, "Electromagnetic diffraction in optical systems," Proc. R. Soc. Lond. A **253**(1274), 358–379 (1959).
39. G.N. Watson, *A Treatise on the Theory of Bessel Functions*, Cambridge University Press, Cambridge (1966).
40. A. Bekshaev, K. Y. Bliokh, and M. Soskin, "Internal flows and energy circulation in light beams," J. Opt. **13**(5), 053001 (2011).
41. V. V. Kotlyar, S. S. Stafeev, and A. G. Nalimov, "Topological Charge of Optical Vortices," Photonics **8**(6), 227 (2021).
42. C. Robens, S. Brakhane, W. Alt, *et al.*, "High numerical aperture (NA = 0.92) objective lens for imaging and addressing of cold atoms," Opt. Lett. **42**(6), 1043–1046 (2017).
43. F. Schreck and K. Druten, "Laser cooling for quantum gases," Nat. Phys. **17**(12), 1296–1304 (2021).
44. A. Vukics, G. Kónya, and P. Domokos, "The gauge-invariant Lagrangian, the Power–Zienau–Woolley picture, and the choices of field momenta in nonrelativistic quantum electrodynamics," Sci. Rep. **11**(1), 16337 (2021).
45. A. Alexandrescu, E. Di Fabrizio, and D. Cojoc, "Electronic and centre of mass transitions driven by Laguerre–Gaussian beams," J. Opt. B: Quantum Semiclass. Opt. **7**(4), 87–92 (2005).
46. S. J. Evered, D. Bluvstein, M. Kalinowski, *et al.*, "High-fidelity parallel entangling gates on a neutral-atom quantum computer," Nature **622**(7982), 268–272 (2023).
47. T. M. Graham, G. Y. Song, J. Scott, *et al.*, "Multi-qubit entanglement and algorithms on a neutral-atom quantum computer," Nature **604**, 457–462 (2022).